



Au-MgF₂-Coated Photonic Crystal Fiber Surface Plasmon Resonance Sensor with High FOM

Yudan Sun¹ · Shimiao Wang² · Qiang Liu² · Shuhui Wei² · Xueyan Zhao² · Tingting Lv² · Jingwei Lv² · Wei Liu² · Paul K. Chu³ · Chao Liu²

Received: 21 December 2023 / Accepted: 5 February 2024
© The Author(s), under exclusive licence to Springer Science+Business Media, LLC, part of Springer Nature 2024

Abstract

A surface plasmon resonance (SPR) sensor composed of photonic crystal fibers (PCFs) is designed for refractive index (RI) sensing with a high figure of merit (FOM). The dual Au-MgF₂ layer is covered on the double-side polished D-type PCF to stimulate SPR. Our numerical analysis reveals that the maximum wavelength sensitivity and amplitude sensitivity of the PCF-SPR sensor are 59,000 nm/RIU and 6076 RIU⁻¹, respectively, in the RI range of 1.25~1.43. The maximum FOM is 2033 RIU⁻¹ and the resolution is 1.69 × 10⁻⁶. The results provide guidance and insights into the design of PCF-SPR sensors with high FOM.

Keywords Surface plasmon resonance · Photonic crystal fiber · Au-MgF₂ · Refractive index sensor

Introduction

Surface plasmon resonance (SPR) is an optical sensing technique offering many advantages such as high sensitivity and real-time detection [1]. Combined with biometric elements, SPR sensors can be used in the analysis of biomolecular interactions [2, 3]. However, conventional SPR sensors consist of thin noble metal films deposited on the substrate [4], and the relatively large confinement loss and low penetration depth hamper the detection of biological macromolecules or thick ligand layers. In comparison with the single-mode or multi-mode fibers [5, 6], photonic crystal fibers (PCFs) are regarded to be excellent SPR sensors due to their outstanding characteristics and

design flexibility which enables optimization to enhance the interactions between the sample and light [7]. Hence, owing to the small size and high sensitivity, PCF-SPR sensors have attracted much attention in medical monitoring, biochemical analysis, and food testing [8–10].

In order to improve the performance of PCF-SPR sensors, several methods have been proposed. The main strategies are modification of the PCF structure and selection of different plasmonic materials. PCF structures with different layouts of air holes and polished optical fibers have been suggested, for example, quasicrystal arrangements [11], elliptical air holes [12], rectangular air holes, and U-shape [13], V-shape [14], D-shape [15], and multi-shape [16] PCFs. Spurred by recent development of coating technology and new materials, PCF-SPR structures are no longer limited to single-layer metals such as gold or silver. Metal oxides like titanium dioxide (TiO₂), zinc oxide (ZnO), and magnesium fluoride (MgF₂) can be combined with metal layers to form multi-layer coatings to improve the sensing properties.

Singh and Prajapati have proposed a gold/MoS₂/graphene D-shape PCF refractive index (RI) sensor [17]. In this device, graphene is deposited to mitigate oxidation and offer better analyte adsorption. Owing to the high surface adsorption efficiency and excellent bandgap tunability of MoS₂, the wavelength sensitivity and FOM are 14,933.34 nm/RIU and 401.05 RIU⁻¹, respectively. Liang et al. have analyzed a D-type PCF-SPR refractive index sensor consisting of a

✉ Chao Liu
msm-liu@126.com

¹ College of Mechanical and Electrical Engineering, Daqing Normal University, Daqing 163712, People's Republic of China

² School of Physics and Electronic Engineering, Northeast Petroleum University, Daqing 163318, People's Republic of China

³ Department of Physics, Department of Materials Science and Engineering, and Department of Biomedical Engineering, City University of Hong Kong, Tat Chee Avenue, Kowloon, Hong Kong, China

silver-graphene/ZnO double-layer composite film [18] and demonstrated sensitivity and resolution of 6000 nm/RIU and 1.667×10^{-5} , respectively. Wang et al. have reported a PCF-SPR sensor with Au-Ta₂O₅ and Ag-Ta₂O₅ coatings for dual analyte detection [19]. The Ta₂O₅ film shifts the working wavelength to the near-infrared region and strengthens the penetrating ability, consequently improving the sensing properties. However, the wavelength sensitivity and resolution are only 11,466 nm/RIU and 8.6×10^{-6} . Islam et al. have designed Au-TiO₂-based PCF-SPR sensors comprising ultra-small air holes for the four coupling channels [20] showing a figure of merit (FOM) of 509.27 RIU⁻¹. In order to simultaneously detect two refractive indexes (RIs), an asymmetric dual RI D-type PCF-SPR sensor has been designed by Wang et al. [21]. In this asymmetric structure, Ag-TiO₂ and Ag-ZrO₂ are the dielectric materials and the wavelength sensitivity of the dual channel is 11,200 nm/RIU and 14,300 nm/RIU.

In this work, a novel symmetrical D-shape PCF-SPR sensor with Au-MgF₂ double-layer film is proposed for refractive index (RI) sensing. The symmetrical D-shape PCF can enhance the coupling between the core mode and SPP mode; meanwhile, the novel Au-MgF₂ double-layer film structure can effectively narrow the full width at half maximum (FWHM) of the loss spectrum and then improve the resolution and FOM of the sensor. The sensor is numerically simulated by the finite element method (FEM) using the COMSOL Multiphysics software. A circular perfect matching layer (PML) is employed as absorbing boundary condition, and the free triangle meshes are adopted in the simulation. A maximum wavelength sensitivity of 59,000 nm/RIU and amplitude sensitivity of 6076 RIU⁻¹ are demonstrated.

Design and Theory

Sensor Structure

Figure 1a depicts the sectional view of the PCF-SPR sensor, and the PCF structure is depicted in Fig. 1b. The radius *R* of the PCF is 5.5 μm. The central air hole is

removed to form the fiber core, while the four air holes in the first layer are replaced by two air holes to expand the coupling channel between the core and plasmonic film. Then, the PCF is designed as double-side D-shaped structure, which can be produced by polishing, and the height *h* is 4.2 μm. The MgF₂ can better adhere to the surface of Au film, increases the penetration depth of electric field in the sensing medium, and enhances the interaction between plasmons and analyte, thus improving the performance of the proposed PCF-SPR sensor. The Au-MgF₂ film with a total thickness of *t* = 44 nm and width of *w* = 7 μm can be deposited by magnetron sputtering or chemical vapor deposition (CVD) [22]. The distance Λ between two adjacent air holes is 2.2 μm, and the diameter of the uniform air hole *d* is 1.1 μm. The outer layer is the perfectly matched layer (PML) to absorb incident light.

The sensor is made of fused silica, and the dispersion relationship is given by the Sellmeier equation [23]:

$$n(\lambda) = \sqrt{1 + \frac{0.6961663\lambda^2}{\lambda^2 - 0.0684043^2} + \frac{0.4079426\lambda^2}{\lambda^2 - 0.1162414^2} + \frac{0.8974794\lambda^2}{\lambda^2 - 9.896161^2}} \quad (1)$$

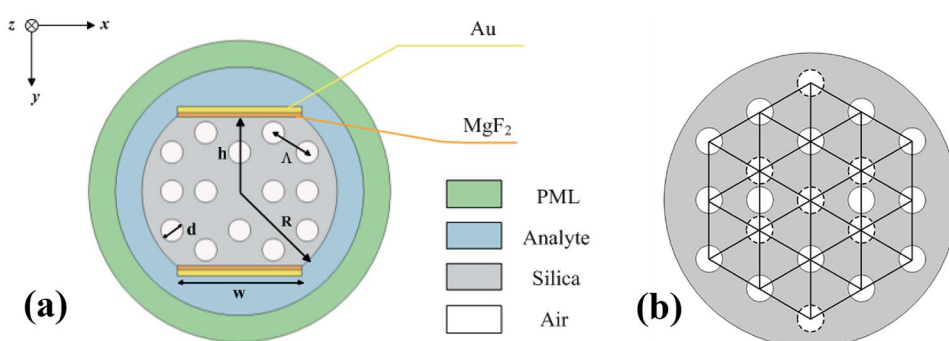
where λ is the wavelength of the incident light in vacuum. Au is considered the ideal plasmonic material due to its high chemical stability. The complex dielectric permittivity can be calculated using the Drude-Lorentz model [24]:

$$\epsilon_{Au} = \epsilon_{\infty} - \frac{\omega_p^2}{\omega^2 + i\omega\omega_{\tau}} \quad (2)$$

where $\omega_p = 1.36 \times 10^{16}$ (rad/s) and $\omega_{\tau} = 1.45 \times 10^{14}$ (rad/s) are the plasmonic frequency and scattering frequency of electrons, respectively. The dielectric constant ϵ_{∞} at high frequencies is 9.75, $\omega = 2\pi c/\lambda$ stands for the angular frequency of incident light, and ϵ_{Au} is the permittivity of the gold film. Therefore, the complex dielectric permittivity ϵ_{Au} changes with the incident wavelength. The refractive index of MgF₂ is described by [25]

$$n_{MgF_2}(\lambda) = \sqrt{1 + \sum_{i=1}^3 \frac{C_i \lambda^2}{\lambda^2 - \lambda_i^2}} \quad (3)$$

Fig. 1 **a** Cross-section of the PCF-SPR sensor and **b** structure of PCF



where $C_1=0.48755108$, $C_2=0.39875031$, $C_3=2.3120353$, $\lambda_1=0.04338408$, $\lambda_2=0.09461442$, and $\lambda_3=23.793604$.

Analysis of the Sensor

The confinement loss affects the PCF-SPR sensor and is defined by the following equation [10]:

$$\alpha_{CL}(dB/cm) = \frac{20}{\ln(10)} \times \frac{2\pi}{\lambda} \times \text{Im}(n_{\text{eff}}) \times 10^4 \quad (4)$$

where $\text{Im}(n_{\text{eff}})$ refers to the imaginary part of the effective RI. Figure 2a shows the dispersion relationship and confinement loss spectra of the sensor when the analyte RI is $n_a=1.40$. The red solid curve and dashed curve represent the real part of the effective RI of the y-polarized core mode and SPP mode, respectively. At the intersection point, the phase-matching conditions for surface plasmon resonance

are satisfied, and the energy of the core mode transfers gradually to the SPP mode as shown in Fig. 2b. Therefore, the confinement loss spectrum shows a loss peak. The black solid line describes the confinement loss of the y-polarized fundamental mode, and similarly, the confinement loss of the x-polarized fundamental mode is shown by the blue solid line. The SPR effect of y-polarization is stronger than that of x-polarization, and more energy couples to SPP mode. Therefore, the electric field intensity of y-polarization is smaller than that of x-polarization, as shown in Fig. 2b and c, and y-polarization is chosen in our subsequent analysis.

Minor variations in the analyte refractive index change the effective refractive index of the SPP mode resulting in a shift in the phase-matching point. It means that the loss spectrum will change with the analyte refractive index. The resonant peak wavelength of the loss spectrum can be used to measure the refractive index of the analyte. As shown in Fig. 3a, the loss spectra exhibit redshift as the

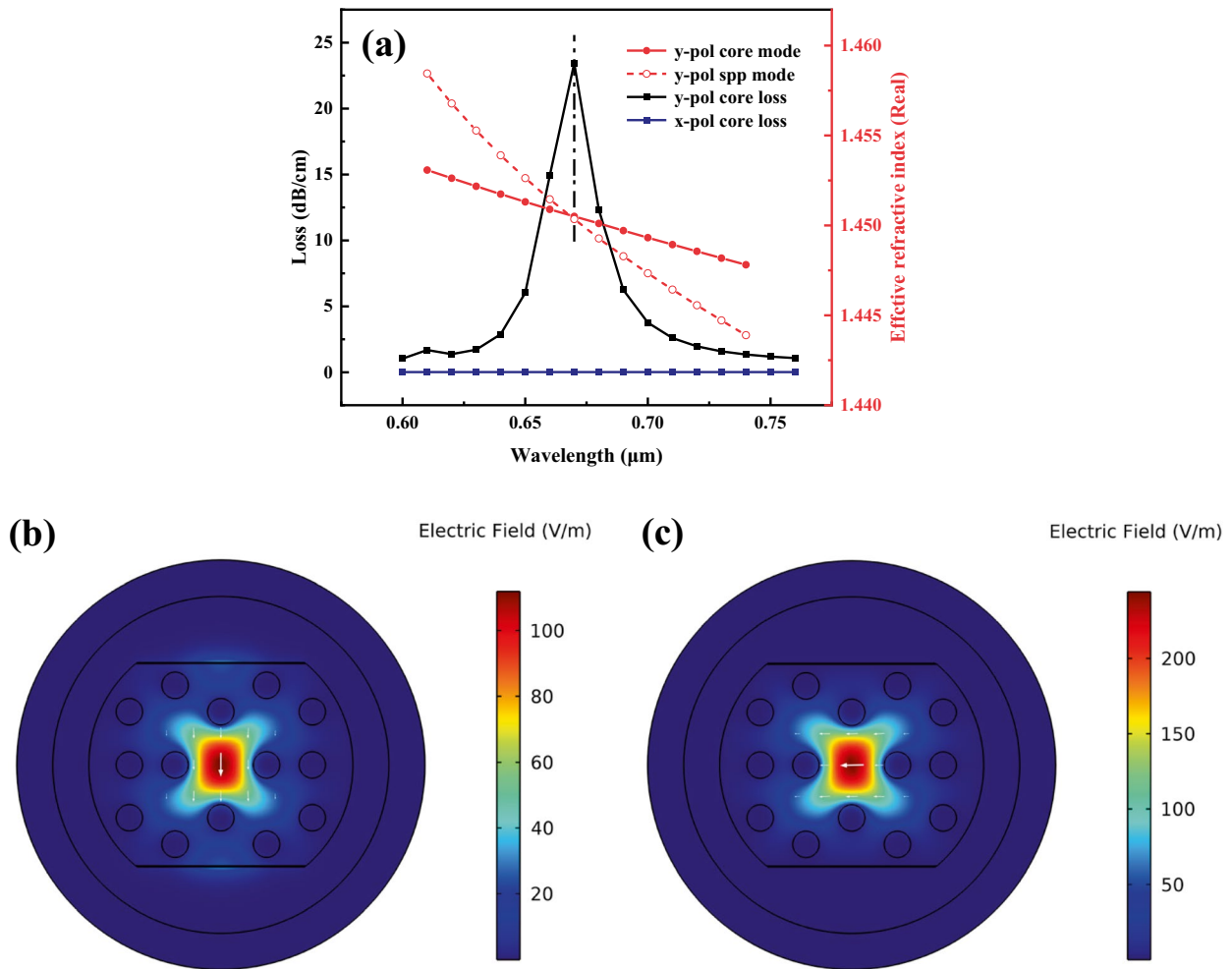


Fig. 2 Dispersion relationship of the core mode and SPP mode for the analyte RI $n_a=1.40$: **a** confinement loss spectra, **b** electric field distribution of y-polarization, and **c** electric field distribution of x-polarization at the phase-matching point

refractive indexes of the analyte increase. Since the core mode is confined in the fiber core, its effective refractive index is not influenced by the analyte. But the real part of the effective indexes of the SPP mode increases with increasing analyte RIs. Therefore, the phase-matching intersection shifts to a longer wavelength. The fitted polynomial curve of the resonant wavelength versus analyte RI is depicted in Fig. 3c. It can be seen that the resonance wavelengths increase slowly in the RI range of 1.25–1.42 and then increase rapidly. This is because the refractive index difference between the core mode and SPP mode decreases significantly with the increase of analyte RI, resulting in the dramatic increase of the resonance wavelength [26]. In addition, the limitation of the PCF structure on the core mode decreases with increasing wavelengths, leading to enhanced surface plasmon resonance effects. Therefore, the peak loss increases gradually. The wavelength offset of the loss peak is utilized to estimate the wavelength sensitivity of the sensor by the following relationship [27]:

$$S_w(nm/RIU) = \frac{\Delta\lambda_p}{\Delta n_a} \tag{5}$$

where Δn_a is the change of the analyte RI and $\Delta\lambda_p$ is the wavelength shift of the loss peak. It is noted that the bimodal spectrum appears as RI = 1.43. The two peaks are caused by complete coupling and incomplete coupling between the core mode and SPP mode [28]. The resolution of the PCF-SPR sensor is defined as follows [29]:

$$R = \frac{\Delta n_a \times \Delta\lambda_{\min}}{\Delta\lambda_p} \tag{6}$$

where $\Delta\lambda_{\min}$ is the minimum wavelength resolution which is set to be 0.1 nm.

The amplitude interrogation method is adopted to determine the properties of the sensor, and the expression is shown in the following [30]:

$$S_a(RIU^{-1}) = -\frac{1}{\alpha_{CL}} \times \frac{\Delta\alpha_{CL}}{\Delta n_a} \tag{7}$$

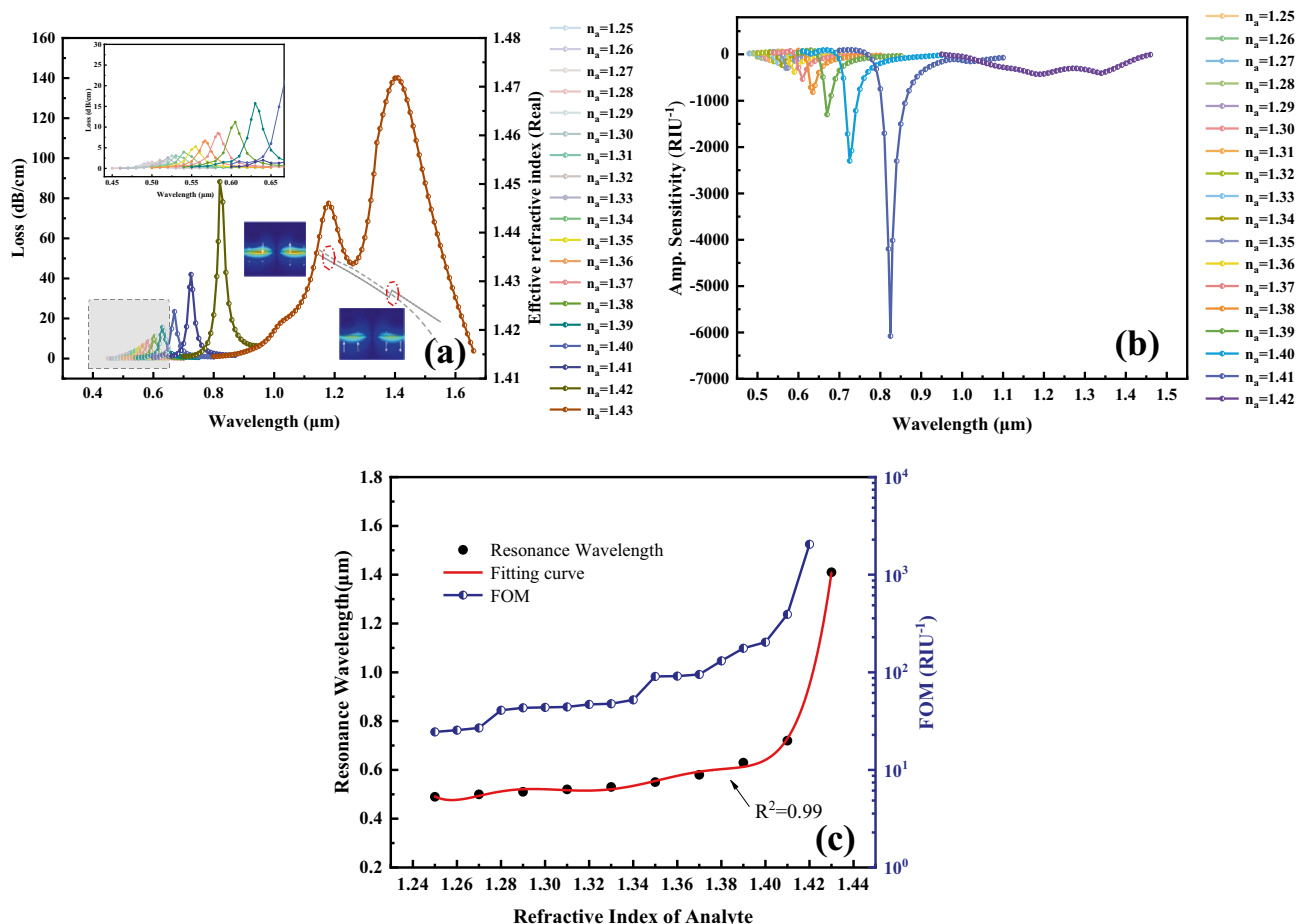


Fig. 3 **a** Confinement loss spectra and **b** amplitude sensitivity for different analyte RIs. **c** Fitted polynomial curve of the resonance wavelengths and FOM for different analyte RIs

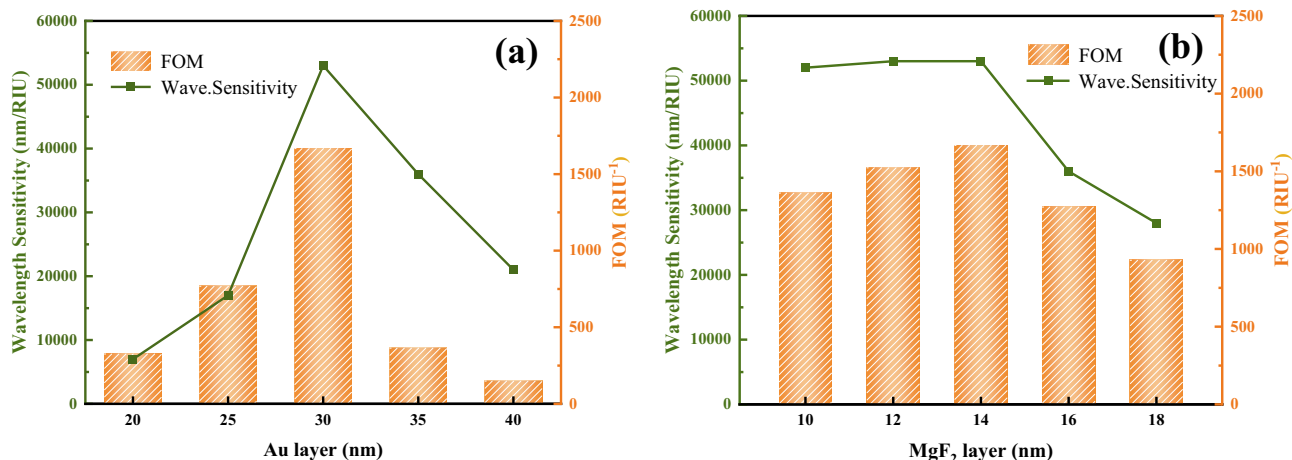


Fig. 4 Wavelength sensitivity and FOM for different thicknesses: a Au layer and b MgF₂ layer

where α_{CL} is the loss at the wavelength and $\Delta\alpha_{CL}$ is the loss difference between two adjacent RIs. The amplitude sensitivity for RIs between 1.25 and 1.41 is shown in Fig. 3b, and it can be inferred that the maximum amplitude sensitivity is 6076 RIU⁻¹ in the RI range of 1.41–1.42.

The figure of merit (FOM) is commonly used to assess the detection accuracy of sensors and is expressed by the following relationship [31]:

$$FOM(RIU^{-1}) = \frac{S_w}{FWHM} \tag{8}$$

where FWHM is the full width at half maximum of the loss spectrum. It means that higher wavelength sensitivity and narrower linewidth represent better sensing properties. The FOM curve for different RIs is displayed in Fig. 3c. The

PCF-SPR sensor exhibits higher FOM that reaches 2033 RIU⁻¹ as the RI is changed from 1.42 to 1.43.

Optimization and Discussion

The structural parameters of the coating materials Au-MgF₂ influence the properties of the sensor. The thicknesses of the Au and MgF₂ films are first optimized. For $t_{MgF_2} = 14$ nm and for Au film thicknesses t_{Au} between 20 and 40 nm, the wavelength sensitivity and FOM are calculated for RI = 1.42 ~ 1.43. As shown in Fig. 4a, the wavelength sensitivity and FOM reach the maximum values when $t_{Au} = 30$ nm. Similarly, Fig. 4b exhibits the wavelength sensitivity and FOM for different t_{MgF_2} of the MgF₂ films with thicknesses between 10 and 18 nm. The properties of the sensor

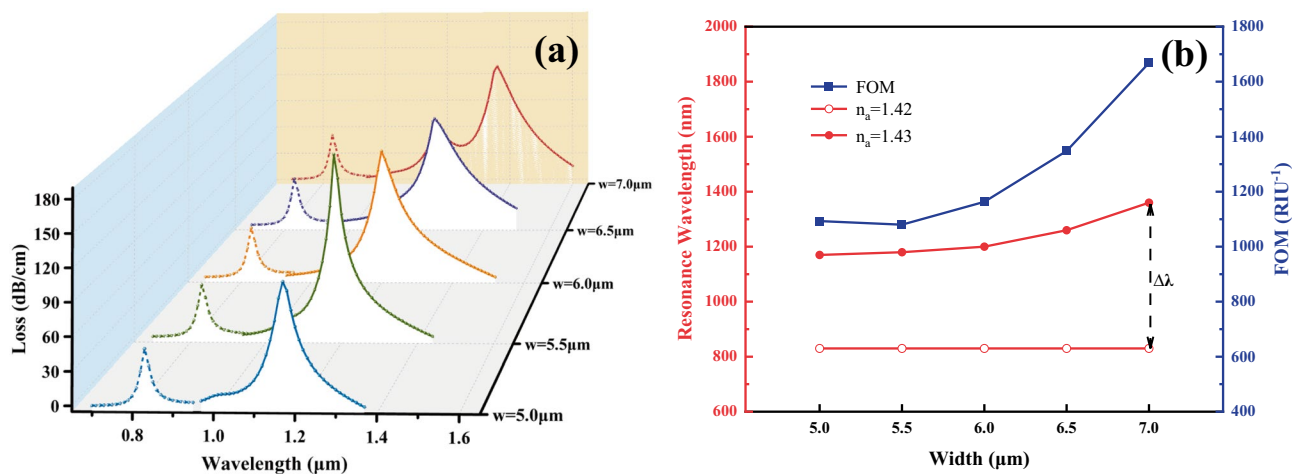


Fig. 5 a Loss spectra for different coating widths and $n_a = 1.42-1.43$ and b resonance wavelengths of the loss spectra for $n_a = 1.42-1.43$ and FOM for $n_a = 1.42$

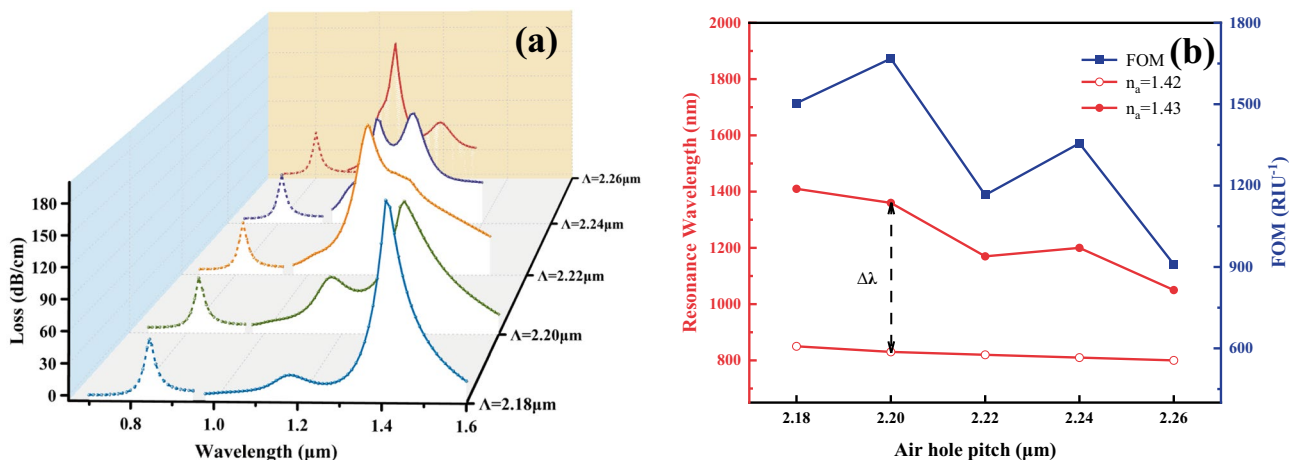


Fig. 6 **a** Loss spectra for different air hole pitches and $n_a = 1.42$ – 1.43 and **b** resonance wavelengths of the loss spectra for $n_a = 1.42$ – 1.43 and FOM for $n_a = 1.42$

are excellent when $t_{MgF_2} = 14$ nm. Because a thicker film weakens the coupling between the core mode and SPP mode [32], $t_{Au} = 30$ nm and $t_{MgF_2} = 14$ nm are selected as the optimal thicknesses.

Figure 5a shows the loss spectra for RI = 1.42 (dashed lines) and RI = 1.43 (solid lines) as the width w of the coating layer is changed from 5.0 to 7.0 μm. When the width increases, the resonance peak of the loss spectra shifts toward a longer wavelength for $n_a = 1.43$, but the resonance wavelength remains basically unchanged for $n_a = 1.42$. Hence, the wavelength sensitivity is improved with increasing w . Figure 5b shows the wavelength shift $\Delta\lambda$ and FOM, and $w = 7$ μm is the optimal width of the coating.

For RIs of 1.42 and 1.43, the loss spectra for different air hole pitches Λ are shown in Fig. 6a and b. The wavelength sensitivity decreases with increasing Λ , and the FOM reaches the maximum of 1668 RIU⁻¹ at $\Lambda = 2.2$ μm.

Therefore, the optimal air hole pitch is determined to be 2.2 μm. The impact of the air hole diameter d on the properties of the sensor (RI = 1.42 ~ 1.43) is illustrated in Fig. 7. With increasing diameter d , the FWHM of the loss spectra widens and the intensity of the resonance coupling decreases when $n_a = 1.42$. It is because a larger diameter d gives rise to better confinement to the core mode. Figure 7b compares the wavelength sensitivity and FOM, and the sensor has the best properties when $d = 1.1$ μm.

On the basis of the aforementioned analysis, the optimal parameters of the PCF-SPR sensor are determined as follows: $w = 7$ μm, $h = 4.2$ μm, $\Lambda = 2.2$ μm, $d = 1.1$ μm, $t_{Au} = 30$ nm, and $t_{MgF_2} = 14$ nm. The properties of our sensor are compared with those of similar sensors, as shown in Table 1. It can be seen that the sensing structure and coating materials directly influence the performance. Compared with other sensors, our sensor shows

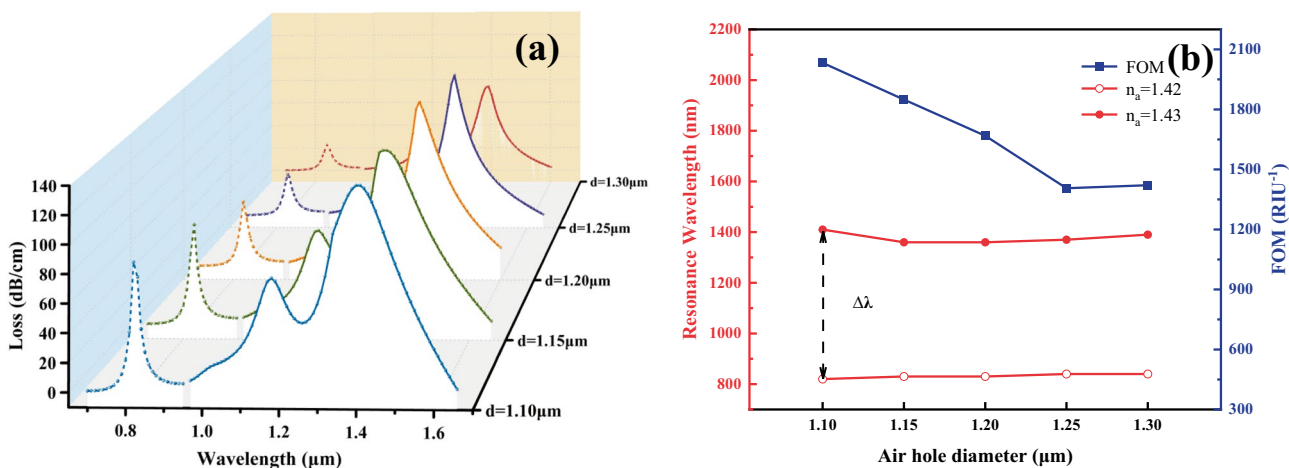


Fig. 7 **a** Loss spectra for different air hole diameters and $n_a = 1.42$ – 1.43 and **b** resonance wavelengths of the loss spectra for $n_a = 1.42$ – 1.43 and FOM for $n_a = 1.42$

Table 1 Comparison of the properties of our sensor and those containing multi-layer coatings reported recently

Refs	Structural design	Coatings	Max Wave. Sens. (nm/RIU)	RI range	Ave. Wave. Sens. (nm/RIU)	Resolution (RIU) (Wave. Int)	Max FOM (RIU ⁻¹)
[33]	PQF-hexagonal	Au-TiO ₂	20,000	1.34–1.38	13,750	5.00×10^{-6}	93.45
[17]	PCF-hexagonal	Au-MoS ₂ -gra	14,933	1.33–1.40	9628	6.69×10^{-6}	401
[34]	PCF-hexagonal	TiO ₂ -Au-gra	48,900	1.32–1.40	13,112	7.60×10^{-6}	611.25
[26]	PCF-hexagonal	Au-AZO	43,600	1.27–1.45	N/A	2.16×10^{-6}	1118
[35]	PCF-rectangular	Au-TiO ₂	40,000	1.32–1.39	14,285	2.50×10^{-6}	N/A
This work	PCF-rectangular and hexagonal	Au-MgF ₂	59,000	1.25–1.43	5389	1.69×10^{-6}	2033

a maximum wavelength sensitivity of 59,000 nm/RIU and FOM of 2033 RIU⁻¹, which are better than those reported recently.

Conclusion

A PCF-SPR sensor with a dual Au-MgF₂ layer is designed and analyzed by the finite element method. The maximum wavelength sensitivity and amplitude sensitivity are 59,000 nm/RIU and 6076 RIU⁻¹, respectively, in the refractive index range of 1.25–1.43. Moreover, the figure of merit (FOM) is improved to 2033 RIU⁻¹. The sensor can thus detect smaller changes in the refractive index of the analyte with a resolution of 1.69×10^{-6} RIU. This PCF-SPR sensor has large application potential in RI sensing, and the strategy also provides insights into the future development of RI sensors with high resolution.

Author Contribution Conceptualization: YS, SWa. Methodology: YS, QL. Formal analysis and investigation: SWa, SWe, XZ. Writing—original draft preparation: SWa. Writing—review and editing: PKC. Funding acquisition: CL. Resources: TL, JL. Validation: WL.

Funding This work was jointly supported by the Instructional Technology Plan of Daqing City (Grant no. zd-2023-19), Daqing Normal University Talent Project (Project no. 22RC006), Basic Research Support Project for the Excellent Youth Scholars of Heilongjiang Province, Heilongjiang Provincial Natural Science Foundation of China (Grant no. JQ2023F001), Local Universities Reformation and Development Personnel Training Supporting Project from Central Authorities, Natural Science Foundation of Heilongjiang Province (Grant no. LH2021F007), China Postdoctoral Science Foundation funded project (Project no. 2020M670881), City University of Hong Kong Strategic Research Grant (SRG) (Grant no. 7005505), and City University of Hong Kong Donation Research Grant (Grant no. DON-RMG 9229021).

Data Availability Due to personal privacy and intellectual property protection, the datasets generated and analyzed during the current study are not publicly available but are available from the corresponding author on reasonable request.

Declarations

Competing Interests The authors declare no conflicts of interest.

References

- Liu Q, Sun JD, Sun YD, Ren ZH, Liu C, Lv JW, Wang FM, Wang LY, Liu W, Sun T, Chu PK (2020) Surface plasmon resonance sensor based on photonic crystal fiber with indium tin oxide film. *Opt Mater* 102:1–8. <https://doi.org/10.1016/j.optmat.2020.109800>
- Zhang P, Liu L, He Y, Ji Y, Guo J, Ma H (2015) Temperature-regulated surface plasmon resonance imaging system for bioaffinity sensing. *Plasmonics* 11:771–779. <https://doi.org/10.1007/s11468-015-0108-y>
- Hinman SS, McKeating KS, Cheng Q (2017) Surface plasmon resonance: material and interface design for universal accessibility. *Anal Chem* 90:19–39. <https://doi.org/10.1021/acs.analchem.7b04251>
- Srivastava A, Verma A, Prajapati YK (2021) Theoretical study of hazardous carbon-di-oxide gas sensing using MIM structure-based SPR sensing scheme. *IET Optoelectron* 15:167–177. <https://doi.org/10.1049/ote.2.12035>
- Fakhri MA, Salim ET, Tariq SM, Ibrahim RK, Alsultany FH, Alwahib AA, Alhasan SFH, Gopinath SCB, Salim ZT, Hashim U (2023) A gold nanoparticles coated unclad single mode fiber-optic sensor based on localized surface plasmon resonance. *Sci Rep* 13:5680. <https://doi.org/10.1038/s41598-023-32852-6>
- Kawata S, Tsai DP, Zuppella P, Corso AJ, Pelizzo MG, Cennamo N, Zeni L (2016) Refractometers for different refractive index range by surface plasmon resonance sensors in multimode optical fibers with different metals. *Plasmonics: Design, Materials, Fabrication, Characterization, and Applications XIV* 9921:1–6. <https://doi.org/10.1117/12.2238143>
- Chaudhary VS, Kumar D, Pandey BP, Kumar S (2023) Advances in photonic crystal fiber-based sensor for detection of physical and biochemical parameters—a review. *IEEE Sens J* 23:1012–1023. <https://doi.org/10.1109/jsen.2022.3222969>
- Yasli A (2021) Cancer detection with surface plasmon resonance-based photonic crystal fiber biosensor. *Plasmonics* 16:1605–1612. <https://doi.org/10.1007/s11468-021-01425-6>
- Thenmozhi H, Mani Rajan MS, Ahmed K (2019) D-shaped PCF sensor based on SPR for the detection of carcinogenic agents in food and cosmetics. *Optik* 180:264–270. <https://doi.org/10.1016/j.ijleo.2018.11.098>
- Liu W, Liu C, Wang J, Lv J, Lv Y, Yang L, An N, Yi Z, Liu Q, Hu C, Chu PK (2023) Surface plasmon resonance sensor composed of microstructured optical fibers for monitoring of external and internal environments in biological and environmental sensing. *Results Phys* 47:1–11. <https://doi.org/10.1016/j.rinp.2023.106365>
- Liu Q, Zhao J, Sun Y, Liu W, Liu C, Lv J, Lv T, Jiang Y, Li B, Wang F, Sun T, Chu PK (2021) High-sensitivity methane sensor composed of photonic quasi-crystal fiber based on surface plasmon resonance. *J Opt Soc Am A*: 38:1438–1442. <https://doi.org/10.1364/JOSAA.432045>

12. Wu JJ, Dou C, Hu LC (2021) The D-shape elliptical stoma photonic crystal fiber based on surface plasmon resonance with both filtering and sensing. *Opt Quant Electron* 53:1–14. <https://doi.org/10.1007/s11082-021-03044-1>
13. Liu Q, Jiang Y, Sun Y, Hu C, Sun J, Liu C, Lv J, Zhao J, Yi Z, Chu PK (2021) Surface plasmon resonance sensor based on U-shaped photonic quasi-crystal fiber. *Appl Opt* 60:1761–1766. <https://doi.org/10.1364/AO.419518>
14. Lv JW, Wang FM, Hu CJ, Yang L, Fu HH, Zeng YS, Chu PK, Liu C (2022) Numerical analysis of multifunctional biosensor with dual-channel photonic crystal fibers based on localized surface plasmon resonance. *Coatings* 12:1–11. <https://doi.org/10.3390/coatings12060742>
15. Liu W, Hu C, Zhou L, Yi Z, Liu C, Lv J, Yang L, Chu PK (2022) A square-lattice D-shaped photonic crystal fiber sensor based on SPR to detect analytes with large refractive indexes. *Physica E* 138:1–8. <https://doi.org/10.1016/j.physe.2021.115106>
16. Singh S, Prajapati YK (2022) Antimonene-gold based twin-core SPR sensor with a side-polished semi-arc groove dual sensing channel: an investigation with 2D material. *Opt Quant Electron* 54:1–14. <https://doi.org/10.1007/s11082-021-03505-7>
17. Singh S, Prajapati YK (2019) Dual-polarized ultrahigh sensitive gold/MoS₂/graphene based D-shaped PCF refractive index sensor in visible to near-IR region. *Opt Quant Electron* 52:1–15. <https://doi.org/10.1007/s11082-019-2122-3>
18. Liang H, Shen T, Feng Y, Liu H, Han W (2020) A D-shaped photonic crystal fiber refractive index sensor coated with graphene and zinc oxide. *Sensors* 21:1–16. <https://doi.org/10.3390/s21010071>
19. Wang S, Ma W, Cheng Q, Liu N, Lu Y, Wu X, Xiang J (2021) Dual-channel surface plasmon resonance-based photonic crystal fiber sensor with metal-Ta₂O₅ coating at near-infrared wavelength. *Plasmonics* 17:119–129. <https://doi.org/10.1007/s11468-021-01503-9>
20. Islam MR, Khan MMI, Siraz S, Mehjabin F, Rahman M, Islam M, Anzum MS, Chowdhury JA, Noor F (2021) Design and analysis of a QC-SPR-PCF sensor for multipurpose sensing with supremely high FOM. *Appl Nanosci* 12:29–45. <https://doi.org/10.1007/s13204-021-02150-6>
21. Wang D, Zhang S, Li Y, Li J (2022) Highly efficient asymmetric dual refractive index D-type photonic crystal fiber surface plasmon resonance sensor. *Plasmonics* 17:2063–2074. <https://doi.org/10.1007/s11468-022-01694-9>
22. Das S, Guha S, Das PP, Ghadai RK (2020) Analysis of morphological, microstructural, electrochemical and nano mechanical characteristics of TiCN coatings prepared under N₂ gas flow rate by chemical vapour deposition (CVD) process at higher temperature. *Ceram Int* 46:10292–10298. <https://doi.org/10.1016/j.ceramint.2020.01.023>
23. Ghosh G, Endo M, Iwasaki T (1994) Temperature-dependent Sellmeier coefficients and chromatic dispersions for some optical fiber glasses. *J Lightwave Technol* 12:1338–1342. <https://doi.org/10.1109/50.317500>
24. Vial A, Grimault A-S, Macías D, Barchiesi D, de la Chapelle ML (2005) Improved analytical fit of gold dispersion: application to the modeling of extinction spectra with a finite-difference time-domain method. *Phys Rev B: Condens Matter Mater Phys* 71:1–7. <https://doi.org/10.1103/PhysRevB.71.085416>
25. Zhang H, Chen Y, Feng X, Xiong X, Hu S, Jiang Z, Dong J, Zhu W, Qiu W, Guan H, Lu H, Yu J, Zhong Y, Zhang J, He M, Luo Y, Chen Z (2019) Long-range surface plasmon resonance sensor based on side-polished fiber for biosensing applications. *IEEE J Sel Top Quantum Electron* 25:1–9. <https://doi.org/10.1109/jstqe.2018.2868159>
26. Rakibul Islam M, Iftekher ANM, Anzum MS, Rahman M, Siraz S (2022) LSPR based double peak double plasmonic layered bent core PCF-SPR sensor for ultra-broadband dual peak sensing. *IEEE Sens J* 22:5628–5635. <https://doi.org/10.1109/jsen.2022.3149715>
27. Sui P, Zhang A, Pan F, Chang P, Pan H, Liu F, Wang J, Cao C (2022) High sensitivity refractive index sensor with wide detection range and high linearity based on LSPR in hollow-core anti-resonance fiber. *Opt Laser Technol* 155:1–7. <https://doi.org/10.1016/j.optlastec.2022.108427>
28. Ma Y, Liu F, Ren Q, Zhang H, Zhang A (2023) Dual-band highly-sensitive SPR photonic crystal fiber sensor based on birefringence analysis. *Opt Commun* 532:1–7. <https://doi.org/10.1016/j.optcom.2022.129253>
29. Islam N, Faizul Huq Arif M, Abu Yousuf M, Asaduzzaman S (2023) Highly sensitive open channel based PCF-SPR sensor for analyte refractive index sensing. *Results Phys* 46:1–11. <https://doi.org/10.1016/j.rinp.2023.106266>
30. Gauvreau B, Hassani A, Fassi Fehri M, Kabashin A, Skorobogatiy MA (2007) Photonic bandgap fiber-based surface plasmon resonance sensors. *Opt Express* 15:11413–11426. <https://doi.org/10.1364/oe.15.011413>
31. Liu C, Su W, Liu Q, Lu X, Wang F, Sun T, Chu PK (2018) Symmetrical dual D-shape photonic crystal fibers for surface plasmon resonance sensing. *Opt Express* 26:9039–9049. <https://doi.org/10.1364/OE.26.009039>
32. Mollah MA, Islam MS (2020) Novel single hole exposed-suspended core localized surface plasmon resonance sensor. *IEEE Sens J* 21:2813–2820. <https://doi.org/10.1109/jsen.2020.3023975>
33. Shakya AK, Ramola A, Singh S, Van V (2022) Design of an ultra-sensitive bimetallic anisotropic PCF SPR biosensor for liquid analytes sensing. *Opt Express* 30:9233–9255. <https://doi.org/10.1364/OE.432263>
34. Singh S, Prajapati YK (2020) TiO₂/gold-graphene hybrid solid core SPR based PCF RI sensor for sensitivity enhancement. *Optik* 224:1–10. <https://doi.org/10.1016/j.ijleo.2020.165525>
35. Ramani U, Kumar H, Kumar R, Singh BK, Pandey PC (2023) Rectangular-shape cladding-based photonic crystal fiber surface plasmon resonance-based refractive index sensor. *Plasmonics* 18:921–929. <https://doi.org/10.1007/s11468-023-01820-1>

Publisher's Note Springer Nature remains neutral with regard to jurisdictional claims in published maps and institutional affiliations.

Springer Nature or its licensor (e.g. a society or other partner) holds exclusive rights to this article under a publishing agreement with the author(s) or other rightsholder(s); author self-archiving of the accepted manuscript version of this article is solely governed by the terms of such publishing agreement and applicable law.